Eur. Phys. J. Plus (2026) 141:208
https://doi.org/10.1140/epjp/s13360-026-07426-w

THE EUROPEAN PHYSICAL JOURNAL PLUS

Regular Article

Distributed nonclassical magnon–photon–phonon entanglement without direct cavity coupling

Muqaddar Abbas[1,a], **Ghaisud Din**[2,b], **Saud Owyed**[3,c], **Hamid R. Hamedi**[4,d], **Pei Zhang**[2,e]

[1] Basic Teaching and Research Department, Shenyang Urban Construction University, Shenyang 110167, China
[2] Ministry of Education Key Laboratory for Nonequilibrium Synthesis and Modulation of Condensed Matter, Shaanxi Province Key Laboratory of Quantum Information and Quantum Optoelectronic Devices, School of Physics, Xi'an Jiaotong University, Xi'an 710049, China
[3] Department of Mathematics, College of Sciences, University of Bisha, 61922 Bisha, Saudi Arabia
[4] Institute of Theoretical Physics and Astronomy, Vilnius University, Sauletekio 3, 10257 Vilnius, Lithuania

Received: 27 November 2025 / Accepted: 9 February 2026

Abstract We investigate a hybrid quantum platform composed of three spatially separated cavity–magnon–phonon units, each realized by placing a yttrium iron garnet (YIG) sphere inside an individual microwave cavity. The cavities are mutually uncoupled, and no direct cavity–cavity interaction is introduced. Instead, nonlocal quantum correlations are supplied by externally prepared nonclassical three-mode entangled probe fields that are injected independently into the three cavities and act as a shared quantum resource. Our focus is not on modeling or monitoring the source that generates the entangled probes, but rather on how such injected nonclassical inputs are redistributed and converted into steady-state hybrid entanglement via local magnon–photon and magnon–phonon interactions within each cavity. Treating each subsystem as coupled to an independent Markovian reservoir, we analyze the driven–dissipative dynamics in a linearized quantum Langevin framework and solve the Lyapunov equation for the steady-state covariance matrix. We systematically characterize the distributed entanglement structure among remote magnons (m_1, m_2, m_3), cavity photons (a_1, a_2, a_3), and representative hybrid triplets including (a_1, m_2, m_3), (m_1, b_1, m_2), and (a_1, a_2, b_3). Our results show that robust steady-state tripartite entanglement can be established and maintained under realistic parameters , and that engineered nonclassical probe fields substantially enhance and distribute genuine tripartite entanglement between distant subsystems beyond what is achievable via purely classical phase synchronization. The proposed modular and reconfigurable architecture offers a scalable route toward continuous-variable quantum networks, distributed quantum memories, and hybrid interfaces tailored for quantum transduction applications.

1 Introduction

Minimizing energy dissipation in spin-wave quanta, or magnons, has become a central objective in the development of next-generation quantum technologies [1–7]. This effort is largely motivated by the intrinsically low magnetic damping and high spin density of magnons, which together enable access to strong coupling regimes [8]. Among available magnonic media, yttrium iron garnet (YIG) has emerged as a benchmark material in cavity quantum electrodynamics and a promising platform for quantum information processing [3, 9–11]. YIG-based systems provide a versatile setting to explore the interplay between magnons, phonons, and cavity electromagnetic modes. In particular, the strong interaction between collective spin excitations [12] and cavity photons enables coherent interconversion of different excitation types [8, 13, 14], thereby opening routes toward novel quantum technologies.

Entanglement [15] has emerged as a central resource in quantum information science [16], with its generation, control, and detection increasingly realized in microscopic quantum platforms [16, 17]. At the same time, entanglement is not confined to the microscopic domain; it also manifests in macroscopic systems, where it serves as a powerful probe of fundamental physics and underpins the formulation of key quantum theoretical frameworks [18]. This broad relevance across physical scales highlights its foundational role in modern quantum science. Recent advances in this direction have significantly driven progress in cavity optomechanics and quantum information processing [19]. An experimental realization of optomechanical entanglement involving cavity field modes and a macroscopic mirror was reported by Vitali et al. [20], while entanglement and mechanical squeezing

[a] e-mail: muqaddarabbas@outlook.com (corresponding author)
[b] e-mail: dinghaisud@stu.xjtu.edu.cn
[c] e-mail: saalgamdi@ub.edu.sa
[d] e-mail: hamid.hamedi@tfai.vu.lt
[e] e-mail: zhangpei@mail.ustc.edu.cn

Published online: 27 February 2026

have also been realized in optomechanical settings [21]. A range of further studies on entanglement in cavity optomechanics can be found in Refs. [22–28]. Beyond their fundamental interest, these systems offer promising prospects for practical applications, including high-precision weak-force sensing [29, 30], gravitational-wave detection [31], engineered mechanical oscillators [32], and single-photon detection [19, 33].

In recent years, drawing motivation from cavity optomechanics, a variety of magnomechanical proposals have been introduced to realize bipartite and tripartite entanglement through the coherent coupling of magnon modes with microwave cavity fields in YIG spheres [34]. Along similar lines, configurations consisting of two magnon modes localized in distinct YIG spheres and coupled via a shared microwave cavity mode have also been theoretically investigated [35]. Subsequent studies [36] demonstrated that, within related setups, the strength of both bipartite and tripartite entanglement can be markedly increased by embedding an optical parametric amplifier (OPA) inside a single microwave cavity. More recent work has further revealed that Kerr-type nonlinearities offer an alternative mechanism for enhancing entanglement in these systems [37, 38]. In parallel, periodically driven and non-Hermitian quantum systems have attracted growing attention due to their unconventional topological properties and dynamical control capabilities [39, 40], offering new perspectives for engineering robust quantum states beyond equilibrium settings. Such Floquet-engineered and non-Hermitian approaches provide valuable theoretical insights that complement the exploration of hybrid magnonic platforms. Collectively, these advances establish cavity magnomechanics [38] as a flexible and robust framework for the generation and control of nonclassical states of hybrid light–matter systems [34, 41–44]. The distinctive coupling mechanisms, nonlinear effects, and driven-system concepts in these platforms offer rich opportunities for exploring quantum correlations and advancing emerging quantum technologies based on magnon–photon–phonon interactions.

Within cavity magnomechanical platforms, considerable effort has been devoted to engineering quantum squeezed states of magnons and phonons [45]. One line of work proposes schemes to generate quantum entanglement and realize unidirectional quantum steering among different mode pairs in such systems [46]. Entanglement properties of antiferromagnet–light hybrids have also been examined [47], demonstrating that magnon–magnon entanglement is strengthened when the antiferromagnetic resonance is tuned to the optical field. Moreover, it has been shown that magnon squeezing arising from the intrinsic self-Kerr nonlinearity of magnons can substantially enhance the correlations between the magnon–phonon, magnon–photon, and photon–phonon subsystems [48]. In addition, extensive investigations into entanglement effects within cavity magnomechanical systems have been reported in Refs. [49–53].

Entanglement enhancement in cavity magnomechanical systems has been explored, for instance, by incorporating an OPA into the cavity, which acts as an internal source of squeezing and amplifies quantum correlations between the constituent modes [54]. Along similar lines, it has been demonstrated that a two-mode squeezed vacuum field can efficiently generate entanglement between two microwave cavities through state-swap interactions in a dual microwave cavity–optomechanical configuration [55]. More recently, the role of direct cavity–cavity coupling in controlling both the strength and redistribution of quantum entanglement among different subsystems has been systematically analyzed in multimode magnonic architectures [56].

In this work, we theoretically investigate a hybrid platform consisting of three spatially separated microwave cavities, each containing a single YIG sphere placed at the magnetic antinode of the cavity mode to maximize the light–matter interaction. *The cavities are mutually uncoupled, providing a setting in which any nonlocal quantum correlations originate from the properties of the input fields rather than from direct inter-cavity coupling. We instead concentrate on how the injected quantum correlations are transferred, redistributed, and transformed into steady-state hybrid entanglement via the local magnon–photon and magnon–phonon interactions within each cavity, while each YIG sphere experiences a homogeneous external bias magnetic field that sets the Zeeman splitting required for coherent magnon—photon coupling, while an additional microwave drive (not shown in the schematic) is used to tune the magnon modes and enhance their interaction with the phonon degrees of freedom.* In this configuration, the bias field establishes coherent magnon–photon interaction, the microwave drive tailors the magnon dynamics and effectively strengthens the magnomechanical coupling, and the intrinsic cavity magnetic field governs the photon dynamics while remaining orthogonal to the applied fields.

Within this architecture, we focus on the formation of steady-state tripartite entanglement among the magnon, photon, and phonon modes in each cavity, as well as on the emergence of distributed hybrid correlations across different nodes. We systematically analyze entanglement patterns involving remote magnons, cavity photons, and various tripartite groupings and show how the nonclassical character of the input fields, combined with local hybrid interactions, can substantially enhance and distribute genuine tripartite entanglement across the uncoupled array. Our scheme explicitly exploits nonclassical input light to boost the strength and robustness of steady-state tripartite entanglement in a multi-cavity magnomechanical network, thereby opening a viable route toward distributed quantum networks, quantum memories, and hybrid interfaces for quantum transduction.

In Sect. 2, we present the system and its Hamiltonian. Section 3 provides a brief discussion of the theoretical results. Finally, Sect. 4 concludes the report with a summary of our work.

2 Model

We consider a three-cavity magnomechanical system, schematically shown in Fig. 1, where each microwave cavity hosts a single YIG sphere of diameter 250 μm [57]. In each sphere, magnon modes arise as collective spin excitations generated by the magnetic

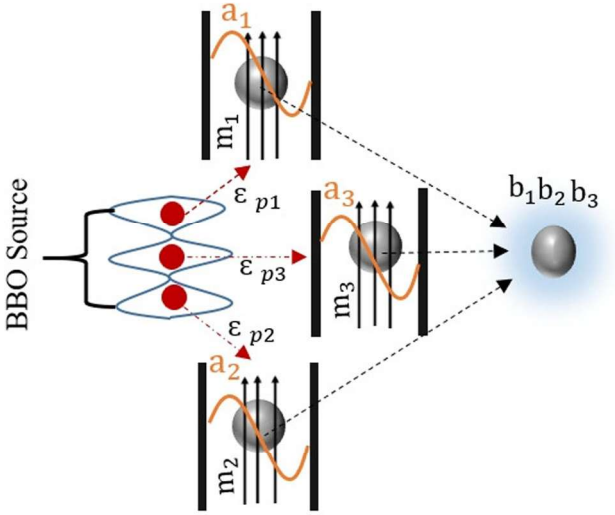

Fig. 1 Schematic illustration of the tripartite entanglement process involving three entangled probe fields generated via parametric down-conversion in a nonlinear BBO crystal. The resulting entangled squeezed fields are individually injected into three separate cavities, labeled a_1, a_2, and a_3, each containing a YIG (yttrium iron garnet) sphere positioned at the magnetic antinode of the corresponding cavity mode to maximize magnon–photon coupling. The arrows denote externally applied static bias magnetic fields (B_{bias}), oriented to facilitate hybridization between cavity photons and collective spin excitations (magnons) within each YIG sphere

interactions between atomic magnetic moments in the crystal lattice [58]. The characteristics of these magnon modes, such as their frequencies and spatial profiles are determined by the crystal structure, the strength of the spin–spin interactions, and the externally applied bias magnetic field. Similarly, phonon modes correspond to quantized lattice vibrations, which can be classified (e.g., longitudinal, transverse, acoustic) according to their frequency and propagation direction, and are likewise shaped by the underlying crystal and magnetic properties of YIG.

For a YIG sphere of diameter 250 μm, the magnon Kerr coefficient is $K_{mi}/2\pi \approx 6.4\times10^{-9}$ Hz. When the condition $K_{mi}|\langle m_i\rangle|^3 \ll \Omega_i$ is satisfied, the Kerr nonlinearity can be safely neglected. In our parameter regime one finds $K_{mi}|\langle m_i\rangle|^3 \approx 5.7\times10^{13}$ Hz and $\Omega_i = 7.1\times10^{14}$ Hz, so that this condition holds and the Kerr term is omitted in what follows.

In the present work, we assume that the three cavity probe fields are prepared in a nonclassical entangled state generated by a common nonlinear, laser-driven source (for instance, an SPDC process in a BBO crystal). *The resulting entangled squeezed fields are individually injected into three separate cavities.* At the level of the mean amplitudes, this corresponds to effective coherent drives with complex strengths $\mathcal{E}_{pi}e^{i\varphi_i}$, as they appear in the Hamiltonian below. *In this approach, the entanglement of the probe fields is treated as an external quantum resource that seeds nonlocal correlations across cavities, while the environmental noise acting on each subsystem remains local and uncorrelated.*

The total Hamiltonian of the three-cavity magnomechanical system, in a suitable rotating frame, can be written as:

$$\begin{aligned}\mathcal{H} = &\sum_{i=1}^{3}\hbar\Delta_{ai}\,a_i^\dagger a_i + \sum_{i=1}^{3}\hbar\Delta_{mi}\,m_i^\dagger m_i + \sum_{i=1}^{3}\hbar\omega_{bi}\,b_i^\dagger b_i \\ &+ \sum_{i=1}^{3}\hbar g_{mai}(a_i^\dagger m_i + a_i m_i^\dagger) + \sum_{i=1}^{3}\hbar g_{mbi}\,m_i^\dagger m_i(b_i + b_i^\dagger) \\ &+ \sum_{i=1}^{3}\mathrm{i}\,\Omega_i(m_i^\dagger - m_i) + \sum_{i=1}^{3}\mathcal{E}_{pi}(a_i^\dagger e^{\mathrm{i}\varphi_i} + a_i e^{-\mathrm{i}\varphi_i}),\end{aligned} \tag{1}$$

where a_i ($a_i^\dagger$), m_i ($m_i^\dagger$), and b_i ($b_i^\dagger$) denote, respectively, the annihilation (creation) operators of the cavity photon, magnon, and phonon modes in the ith cavity; $\Delta_{ai} = \omega_{ai} - \omega_{0i}$ and $\Delta_{mi} = \omega_{mi} - \omega_{0i}$ represent the detuning of the cavity and magnon modes; ω_{bi} is the mechanical frequency; g_{mai} and g_{mbi} are the cavity–magnon and magnomechanical coupling strengths; Ω_i is the amplitude of the coherent microwave drive applied to the magnon mode; and $\mathcal{E}_{pi}$ and φ_i describe the effective drive strength and phase of the probe field injected into cavity i. Here, g_{mbi} represents the magnomechanical coupling rate between the magnon and phonon modes, while g_{mai} is the magnon–microwave coupling rate. The Rabi frequency $\Omega = \frac{\sqrt{5}}{4}\gamma\sqrt{N}B_0$ [59] represents the strength of the driving magnetic field with amplitude B_0. Here, $\gamma/2\pi = 28$ GHz/T, $N = \rho V$, where $\rho = 4.22\times10^{27}$ m^{-3} is the spin density and V is the volume of the YIG sphere [60].

After considering the corresponding dissipation and fluctuating terms, the Heisenberg–Langevin equation [62] based on the total Hamiltonian in Eq. (1) reads:

$$\dot{a}_i = -(\mathrm{i}\Delta_{ai} + \kappa_{ai})a_i - \mathrm{i}g_{mai}m_i - i\mathcal{E}_{pi}e^{i\varphi_i} + \sqrt{2\kappa_{ai}}a_i^{in}, \tag{2}$$

$$\dot{m}_i = -(\mathrm{i}\Delta_{mi} + \kappa_{mi})m_i - \mathrm{i}g_{mai}a_i - \mathrm{i}g_{mbi}m_i(b_i + b_i^\dagger) + \Omega_i + \sqrt{2\kappa_{mi}}m_i^{in}, \tag{3}$$

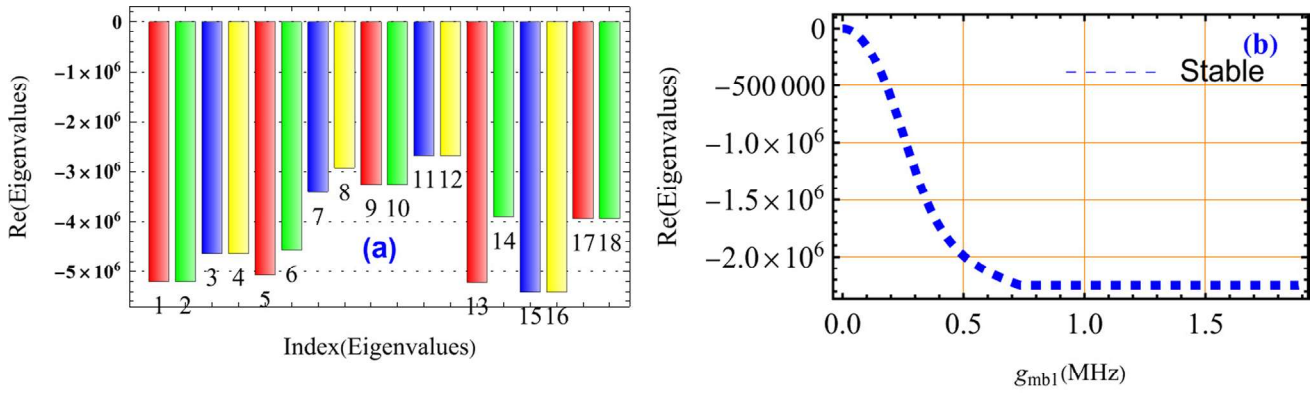

Fig. 2 **a** Real part of the Eigenvalues of the matrix Z for the exact same parameters given in the main text. **b** Maximum real eigenvalue of the matrix Z vs coupling strength g_{mb1}

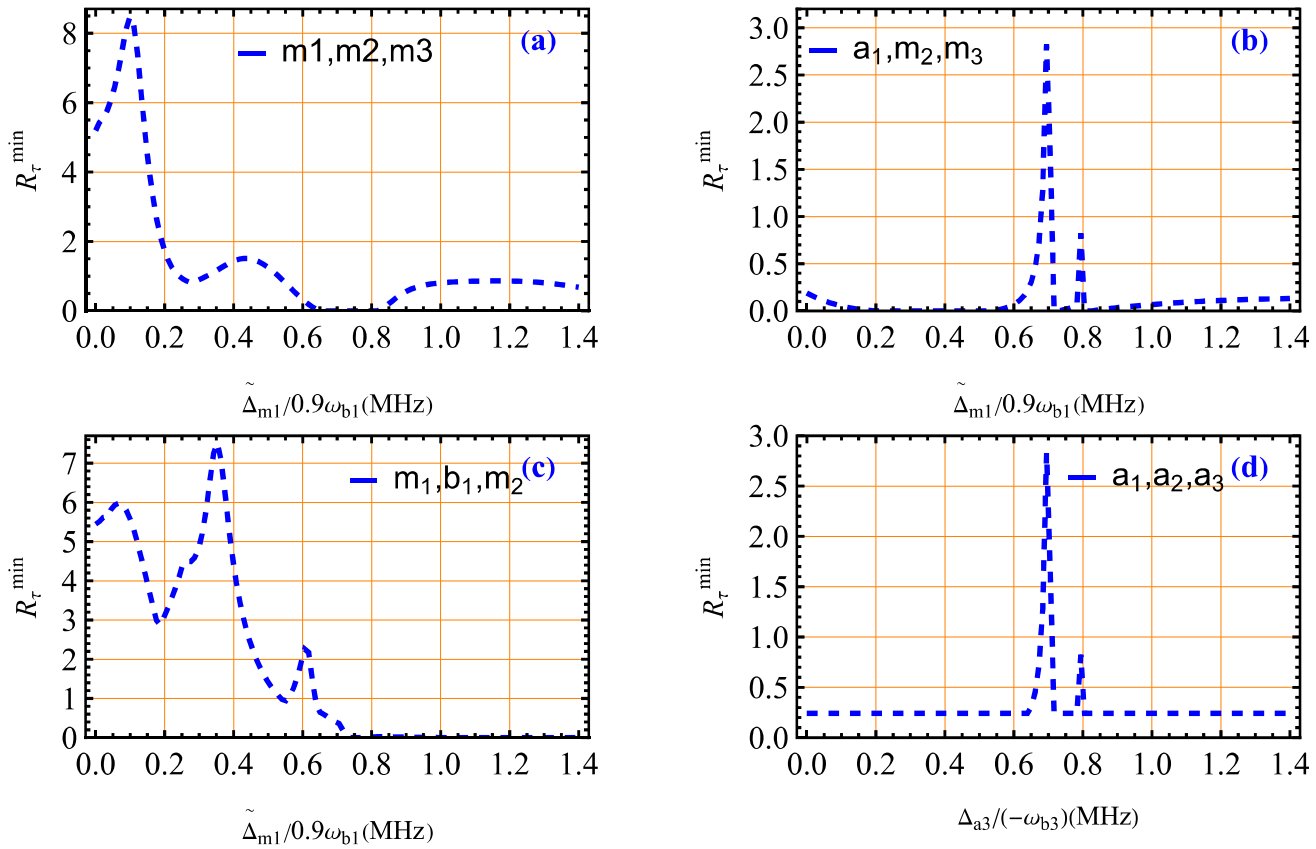

Fig. 3 Plot of the tripartite entanglement $R_\tau^{\min}$ as a function of the effective magnon drive and cavity detuning parameters. Subfigures **a–c** show the variation of $R_\tau^{\min}$ with respect to the normalized detuning $\tilde{\Delta}_{m1}/0.9\omega_{b1}$: **a** magnon–magnon–magnon (m1, m2, m3), **b** cavity—magnon–magnon (a1, m2, m3), **c** magnon–phonon–magnon (m1, b1, m2) entanglement configurations. Subfigure **d** illustrates the cavity–cavity–cavity (a1, a2, a3) tripartite entanglement plotted as a function of the normalized detuning $\Delta_{a3}/(-\omega_{b3})$. The parameters used are: $g_{ma1}/2\pi = 3.2$ MHz, $g_{ma2}/2\pi = 3.0$ MHz, $g_{ma3}/2\pi = 3.2$ MHz, $g_{mbi}/2\pi = 0.3$ Hz, $\omega_{bi}/2\pi = 10$ MHz, $\Omega_i = 7.1 \times 10^{14}$ Hz, $\Delta_{ai} = -\omega_{bi}$, $\tilde{\Delta}_{mi} = 0.9\omega_{bi}$, $\gamma_{bi}/2\pi = 100$ Hz, $\kappa_{ai}/2\pi = 1$ MHz, and $\kappa_{mi}/2\pi = 1$ MHz [34, 61]

$$\dot{b}_i = -(\mathrm{i}\omega_{bi} + \gamma b_i)b_i - \mathrm{i}g_{mbi}m_i^\dagger m_i + \sqrt{2\gamma_{bi}}b_i^{in}. \tag{4}$$

Next, we linearize the equations around the steady-state values, introducing small fluctuations around these values. We achieve this by expressing the operators as $a_i = a_{is} + \delta a_i$, $m_i = \alpha_i + \delta m_i$, and $b_i = b_{is} + \delta b_i$. The resulting fluctuation equations can then be written as:

$$\dot{a}_{is} + \delta\dot{a}_i = -(\mathrm{i}\Delta_{ai} + \kappa_{ai})(a_{is} + \delta a_i) - \mathrm{i}g_{mai}(\alpha_i + \delta m_i) + \sqrt{2\kappa_{ai}}a_i^{in}, \tag{5}$$

$$\dot{\alpha}_i + \delta\dot{m}_i = -(\mathrm{i}\Delta_{mi} + \kappa_{mi})(\alpha_i + \delta m_i) - \mathrm{i}g_{mai}(a_{is} + \delta a_i) - \mathrm{i}g_{mbi}(\alpha_i + \delta m_i)(b_{is} + \delta b_i + b_{is}^{\dagger} + \delta b_i^{\dagger}) + \sqrt{2\kappa_{mi}}m_i^{\mathrm{in}}, \tag{6}$$

$$\dot{b}_{is} + \delta\dot{b}_i = -(\mathrm{i}\omega_{bi} + \gamma_{bi})(b_{is} + \delta b_i) - \mathrm{i}g_{mbi}\left((\alpha_i^{*} + \delta m_i^{*})(\alpha_i + \delta m_i)\right) + \sqrt{2\gamma_{bi}}b_i^{\mathrm{in}}. \tag{7}$$

In Eqs. (5)–(7), a_i^{in}, m_i^{in}, and b_i^{in} represent the input noise operators corresponding to the cavity, magnon, and mechanical modes, respectively. Additionally, γ_{bi} is the damping rate of the mechanical modes. These input noise operators are assumed to have nonzero correlation functions [63].

The noise correlation functions used in our model follow standard quantum Langevin theory and are derived under the assumption of independent, Markovian reservoirs. These correlations take the form:

$$\langle a_i^{in\dagger}(t)a_i^{in}(t')\rangle = \mathcal{N}_{ai}\delta(t-t') \tag{8}$$

$$\langle a_i^{in}(t)a_i^{in\dagger}(t')\rangle = (\mathcal{N}_{ai}+1)\delta(t-t') \tag{9}$$

$$\langle m_i^{in\dagger}(t)m_i^{in}(t')\rangle = N_{mi}\delta(t-t') \tag{10}$$

$$\langle m_i^{in}(t)m_i^{in\dagger}(t')\rangle = (N_{mi}+1)\delta(t-t') \tag{11}$$

$$\langle b_i^{in\dagger}(t)b_i^{in}(t')\rangle = N_{bi}\delta(t-t') \tag{12}$$

$$\langle b_i^{in}(t)b_i^{in\dagger}(t')\rangle = (N_{bi}+1)\delta(t-t') \tag{13}$$

$$\langle a_1^{in}(t)a_2^{in}(t')\rangle = \mathcal{M}_{1,2}\mathrm{Exp}[-i\omega_b(t+t')]\delta(t-t') \tag{14}$$

$$\langle a_2^{in}(t)a_3^{in}(t')\rangle = \mathcal{M}_{2,3}\mathrm{Exp}[-i\omega_b(t+t')]\delta(t-t') \tag{15}$$

$$\langle a_3^{in}(t)a_1^{in}(t')\rangle = \mathcal{M}_{3,1}\mathrm{Exp}[-i\omega_b(t+t')]\delta(t-t') \tag{16}$$

where for $x = m,\ b$, $N_{x_i}(\omega_{x_i}) = [\exp(\hbar\omega_{x_i}/k_B T_{x_i}) - 1]^{-1}$ is the thermal occupation number of the respective bath and

$$\mathcal{N}_{a1} = \sinh(r_{1,2}) + \sinh^2(r_{1,2}) \tag{17}$$

$$\mathcal{N}_{a2} = \sinh(r_{2,3}) + \sinh^2(r_{2,3}) \tag{18}$$

$$\mathcal{N}_{a3} = \sinh(r_{3,1}) + \sinh^2(r_{3,1}) \tag{19}$$

$$\mathcal{M}_{1,2} = \sinh(r_{1,2})\cosh(r_{1,2}) \tag{20}$$

$$\mathcal{M}_{2,3} = \sinh(r_{2,3})\cosh(r_{2,3}) \tag{21}$$

$$\mathcal{M}_{3,1} = \sinh(r_{3,1})\cosh(r_{3,1}) \tag{22}$$

We assume that the three cavity inputs are prepared in a stationary three-mode Gaussian entangled state (e.g., from SPDC in a BBO crystal). These nonclassical correlations are encoded in the input noise covariance matrix and enter the Lyapunov equation via the diffusion matrix D.

The diffusion matrix D is the stationary noise correlation matrix which is defined by $D_{i,j} = 1/2\ n_i(t)n_j(t') + n_j(t')n_i(t)$ *with* $(i,\ j = 1,\ 2,\ 3,\ 4...18)$. *which can be determind by using Eqs.* (8) *to* (16).

Here, a Markov approximation has been made, which is valid when the mechanical quality factor is $Q = \frac{\omega_{bi}}{\gamma_{bi}} \gg 1$ [64].

Since our primary interest lies in the quantum correlation properties of the three-cavity magnon mode system, we focus on the dynamics of its quantum fluctuations. The linearized quantum Langevin equations governing the fluctuations of the system quadratures are given by:

$$\sqrt{2}\delta A_1 = (\delta a_1 + \delta a_1^{\dagger}), \quad \sqrt{2}\delta B_1 = \mathrm{i}(\delta a_1^{\dagger} - \delta a_1), \tag{23}$$

$$\sqrt{2}\delta A_2 = (\delta a_2 + \delta a_2^{\dagger}), \quad \sqrt{2}\delta B_2 = \mathrm{i}(\delta a_2^{\dagger} - \delta a_2), \tag{24}$$

$$\sqrt{2}\delta A_3 = (\delta a_3 + \delta a_3^{\dagger}), \quad \sqrt{2}\delta B_3 = \mathrm{i}(\delta a_3^{\dagger} - \delta a_3), \tag{25}$$

$$\sqrt{2}\delta C_1 = (\delta m_1 + \delta m_1^{\dagger}), \quad \sqrt{2}\delta D_1 = \mathrm{i}(\delta m_1^{\dagger} - \delta m_1), \tag{26}$$

$$\sqrt{2}\delta C_2 = (\delta m_2 + \delta m_2^{\dagger}), \quad \sqrt{2}\delta D_2 = \mathrm{i}(\delta m_2^{\dagger} - \delta m_2), \tag{27}$$

$$\sqrt{2}\delta C_3 = (\delta m_3 + \delta m_3^{\dagger}), \quad \sqrt{2}\delta D_3 = \mathrm{i}(\delta m_3^{\dagger} - \delta m_3), \tag{28}$$

$$\sqrt{2}\delta E_1 = (\delta b_1 + \delta b_1^{\dagger}), \quad \sqrt{2}\delta F_1 = \mathrm{i}(\delta b_1^{\dagger} - \delta b_1), \tag{29}$$

$$\sqrt{2}\delta E_2 = (\delta b_2 + \delta b_2^\dagger), \quad \sqrt{2}\delta F_2 = \mathrm{i}(\delta b_2^\dagger - \delta b_2), \tag{30}$$

$$\sqrt{2}\delta E_3 = (\delta b_3 + \delta b_3^\dagger), \quad \sqrt{2}\delta F_3 = \mathrm{i}(\delta b_3^\dagger - \delta b_3), \tag{31}$$

$$\sqrt{2}A_i^{\mathrm{in}} = (a_i^{\mathrm{in}} + a_i^{\mathrm{in}\dagger}), \quad \sqrt{2}B_i^{\mathrm{in}} = \mathrm{i}(a_i^{\mathrm{in}\dagger} - a_i^{\mathrm{in}}), \tag{32}$$

$$\sqrt{2}C_i^{\mathrm{in}} = (m_i^{\mathrm{in}} + m_i^{\mathrm{in}\dagger}), \quad \sqrt{2}D_i^{\mathrm{in}} = \mathrm{i}(m_i^{\mathrm{in}\dagger} - m_i^{\mathrm{in}}), \tag{33}$$

$$\sqrt{2}E_i^{\mathrm{in}} = (b_i^{\mathrm{in}} + b_i^{\mathrm{in}\dagger}), \quad \sqrt{2}F_i^{\mathrm{in}} = \mathrm{i}(b_i^{\mathrm{in}\dagger} - b_i^{\mathrm{in}}). \tag{34}$$

By substituting the quadratures described above into Eqs. (5), (6), and (7), we derive the following equations:

$$\delta\dot{A}_i = -\kappa_{ai}\delta A_i + \Delta_{ai}\delta B_i + g_{mai}\delta D_i + \sqrt{2\kappa_{ai}}A_i^{\mathrm{in}} \tag{35}$$

$$\delta\dot{B}_i = -\Delta_{ai}\delta A_i - \kappa_{ai}\delta B_i - g_{mai}\delta C_i + \sqrt{2\kappa_{ai}}B_i^{\mathrm{in}} \tag{36}$$

$$\delta\dot{C}_i = -\kappa_{mi}\delta C_i + \tilde{\Delta}_{mi}\delta D_i + g_{mai}\delta B_i + \sqrt{2\kappa_{mi}}C_i^{\mathrm{in}} \tag{37}$$

$$\delta\dot{D}_i = -\tilde{\Delta}_{mi}\delta C_i - \kappa_{mi}\delta D_i - g_{mai}\delta A_i - 2g_{mbi}\alpha_i\delta E_i + \sqrt{2\kappa_{mi}}D_i^{\mathrm{in}} \tag{38}$$

$$\delta\dot{E}_i = -\gamma_{bi}\delta E_i + \omega_{bi}\delta F_i + g_{mbi}(\alpha_i^* - \alpha_i)\delta D_i + \sqrt{2\gamma_{bi}}E_i^{\mathrm{in}} \tag{39}$$

$$\delta\dot{F}_i = -\omega_{bi}\delta E_i - \gamma_{bi}\delta F_i - g_{mbi}(\alpha_i^* + \alpha_i)\delta C_i + \sqrt{2\gamma_{bi}}F_i^{\mathrm{in}} \tag{40}$$

In the above Eqs. (35)–(40), we define

$$\tilde{\Delta}_{mi} = \Delta_{mi} - \frac{2g_{mbi}^2\omega_{bi}|\alpha_i|^2}{\gamma_{bi}^2 + \omega_{bi}^2}, \tag{41}$$

and express the system dynamics using the compact form

$$\dot{u}(t) = Zu(t) + n(t), \tag{42}$$

where u and n are the vectors of the input noise, given in the appendix. *The drift matrix Z provides a compact representation of the linearized dynamics of the quadrature fluctuations. It assumes a block-diagonal structure, with each block describing the local cavity–magnon–phonon subsystem associated with a given node. The nonvanishing coefficients are set by the cavity and magnon dissipation rates, the mechanical damping, the effective detunings, and the linearized magnon–photon and magnon–phonon interaction strengths. Because the Hamiltonian contains no direct cavity–cavity coupling, Z includes no Hamiltonian-generated off-diagonal blocks connecting different nodes. For completeness, we provide the explicit nonzero elements of Z in Appendix A.*

In the elements of the matrix Z given in the appendix, α_i ($i = 1, 2, 3$) can be expressed as:

$$\alpha_i = \frac{\Omega_i}{\tilde{\Delta}_{mi} + \kappa_{mi} + \frac{g_{mai}^2}{\mathrm{i}\Delta_{ai} + \kappa_{ai}}}. \tag{43}$$

The drift matrix is constructed under the assumption that $|\langle\alpha_i\rangle|^2 \gg \kappa_{ai}, \kappa_{mi}$. The dynamical stability of the system is confirmed by ensuring that all eigenvalues possess strictly negative real parts. By further assuming Gaussian quantum noise with vanishing mean values, the steady-state quantum fluctuations form a continuous-variable tripartite Gaussian state within each cavity. This state is completely described by an 18×18 covariance matrix V, whose elements are defined as

$$V_{i,j} = \frac{1}{2}\langle u_i(t)u_j(t') + u_j(t')u_i(t)\rangle, \quad (i, j = 1, 2, \ldots, 18).$$

For a stable system, the covariance matrix is obtained by solving the associated Lyapunov equation,

$$ZV + VZ^T + D = 0, \tag{44}$$

where D denotes the diffusion matrix, the explicit form of which is provided in the Appendix.

The Lyapunov equation is solved numerically; however, owing to the high dimensionality of the resulting covariance matrix, its explicit analytical form is not reported here. To assess and quantify the entanglement between different subsystems, we adopt the logarithmic negativity [65], a standard and widely accepted measure of bipartite entanglement. It is defined as

$$E_N = \max\left[0, -\ln\left(2\chi'\right)\right]. \tag{45}$$

Here, χ' denotes the smallest symplectic eigenvalue of the partially transposed reduced covariance matrix associated with the two subsystems under consideration. In addition to bipartite correlations, this work focuses on genuine tripartite entanglement, which is characterized using the residual contangle R_τ [59, 66].

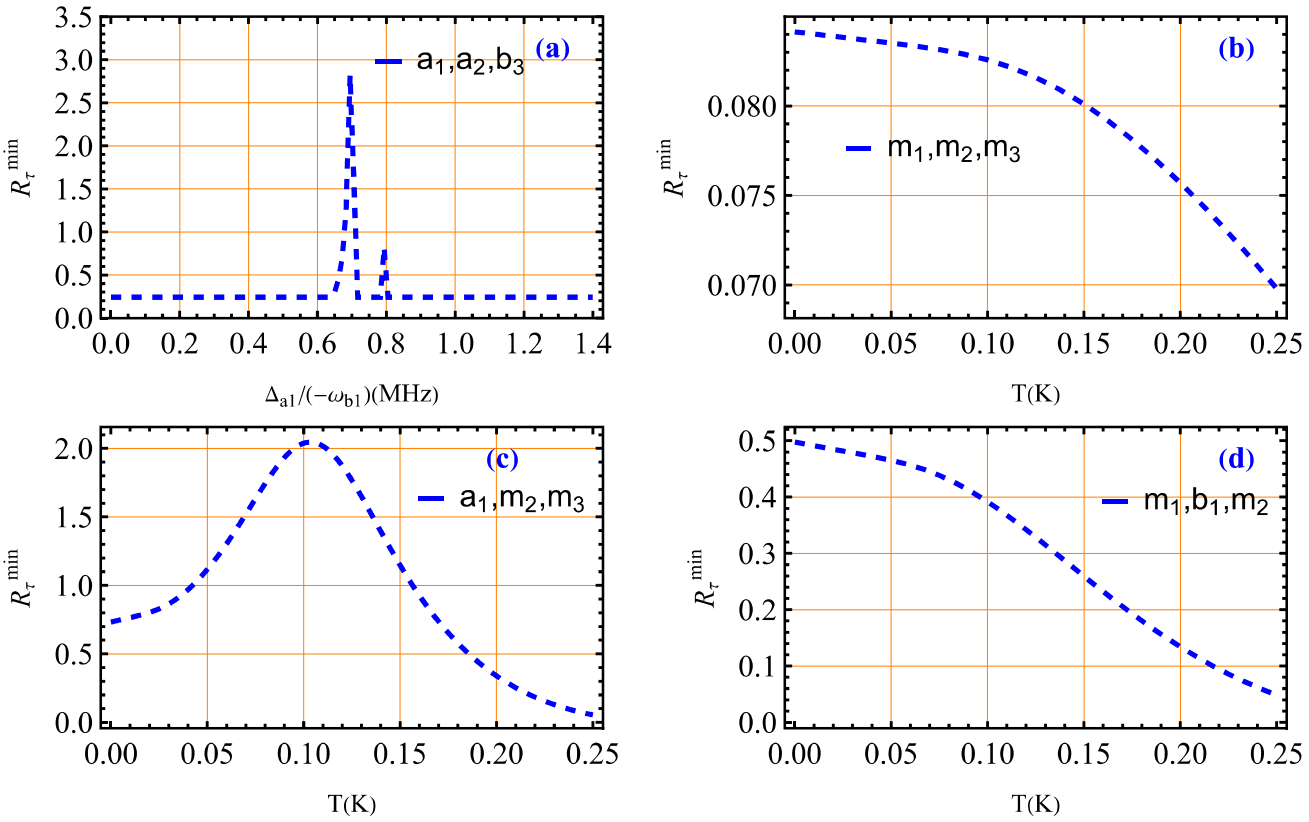

Fig. 4 Plot of the tripartite entanglement $R_\tau^{\min}$ as a function of the cavity detuning $\Delta_{a1}/(-\omega_{b1})$ and temperature T (in Kelvin). Subfigure **a** (a1, a2, b3) shows the variation of $R_\tau^{\min}$ with $\Delta_{a1}/(-\omega_{b1})$ for the cavity—cavity–phonon configuration. Subfigures **b–d** show the variation of $R_\tau^{\min}$ with temperature T for the following configurations: **b** magnon–magnon–magnon (m1, m2, m3), **c** cavity–magnon–magnon (a1, m2, m3), and **d** magnon—phonon—magnon (m1, b1, m2). The occupation numbers are: $N_{bi} = 20.4321$, $N_{mi} = 1.72883 \times 10^{-21}$, with effective magnon detuning $\tilde{\Delta}_{m1} = 0.6\omega_{bi}$. Other parameters are the same as those used in Fig. 3

In continuous-variable quantum systems, particularly those characterized by Gaussian states, the quantification of genuine tripartite entanglement can be achieved using the minimum residual contangle. This method, proposed in Ref. [67], is based on computing the contangle, which is defined as the square of the logarithmic negativity, across all bipartitions of the system.

For a three-mode Gaussian state, the entanglement between one mode and the remaining two is evaluated by partially transposing the corresponding covariance matrix and determining the smallest symplectic eigenvalue. The contangle is then calculated for each of the three possible bipartitions. Rather than subtracting pairwise entanglement contributions, the minimum among these three bipartite contangles is taken as the minimum residual contangle, thereby isolating the genuine tripartite entanglement. For our system, it can be explicitly expressed as

$$\begin{aligned}
R_\tau^{min}(m_1,m_2,m_3) &= \min[R_\tau^{m_1|m_2m_3}, R_\tau^{m_2|m_1m_3}, R_\tau^{m_3|m_1m_2}],\\
R_\tau^{min}(a_1,m_2,m_3) &= \min[R_\tau^{a_1|m_2m_3}, R_\tau^{m_2|a_1m_3}, R_\tau^{m_3|a_1m_2}],\\
R_\tau^{min}(m_1,b_1,m_2) &= \min[R_\tau^{m_1|b_1m_2}, R_\tau^{b_1|m_1m_2}, R_\tau^{m_2|b_1m_1}],\\
R_\tau^{min}(a_1,a_2,a_3) &= \min[R_\tau^{a_1|a_2a_3}, R_\tau^{a_2|a_1a_3}, R_\tau^{a_3|a_1a_2}],\\
R_\tau^{min}(a_1,a_2,b_3) &= \min[R_\tau^{a_1|a_2b_3}, R_\tau^{a_2|a_1b_3}, R_\tau^{b_3|a_1a_2}].
\end{aligned} \tag{46}$$

To clarify the role of the global coherent drive, we emphasize that all three cavities are driven by phase-coherent probe fields derived from a single stabilized source. Although the cavities are not directly coupled in the Hamiltonian, their intracavity fields inherit a common phase reference, leading to synchronized intracavity dynamics. This shared coherence enables the transfer of phase correlations across cavities, which in turn induces intermode quantum correlations. These quantum correlations are revealed in the off-diagonal terms of the steady-state covariance matrix and quantified using the minimum residual contangle. This mechanism goes beyond classical phase-locking, as verified by the vanishing of entanglement when the global coherence is removed. Our results thus indicate that the global drive plays a crucial role in establishing genuine multipartite quantum entanglement across spatially separated systems.

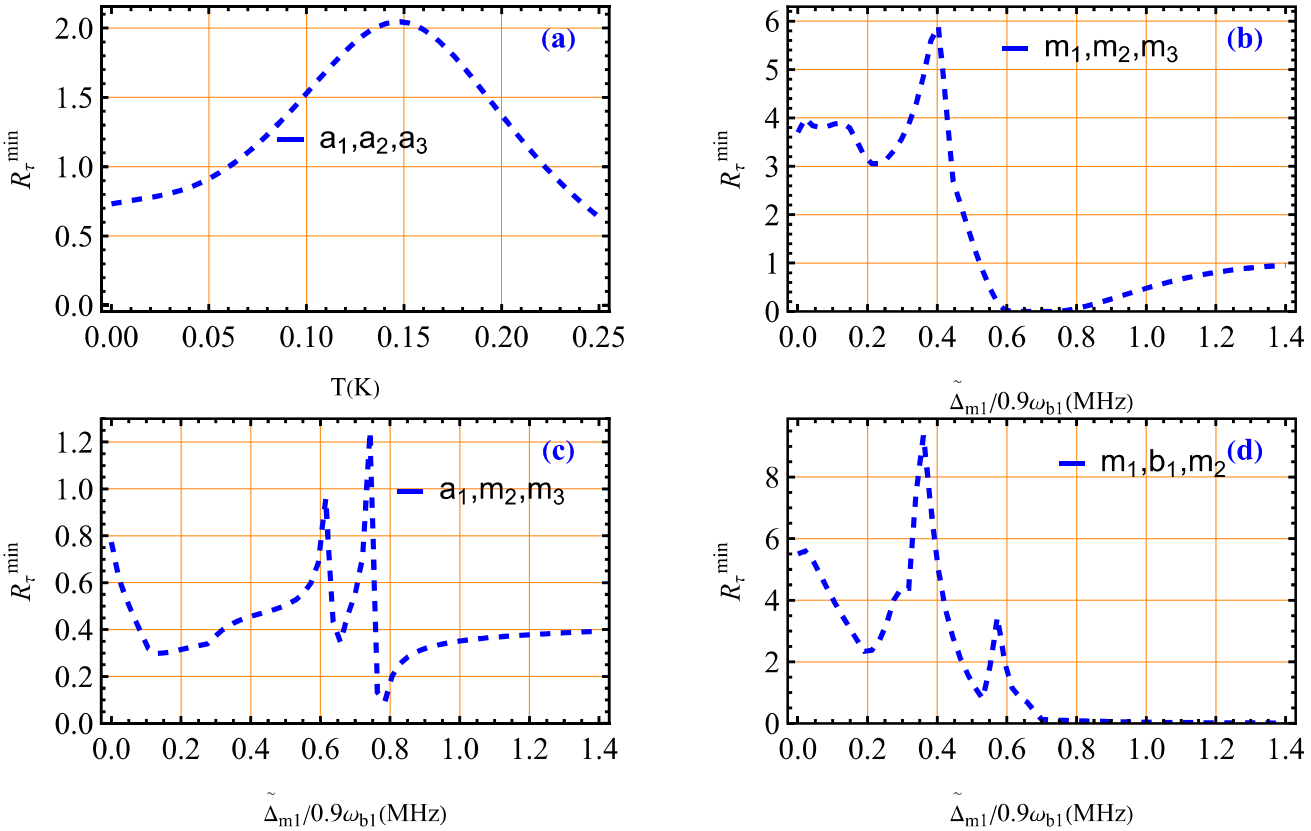

Fig. 5 Plot of the tripartite entanglement $R_\tau^{\min}$ as a function of the effective magnon drive $\tilde{\Delta}_{m1}/(0.9\omega_{b1})$ and temperature $T(K)$. Subfigure **a** shows the tripartite entanglement among cavity modes (cavity—cavity—cavity). The parameters used are the same as in Fig. 5. Subfigures **b–d** present the tripartite entanglement for **b** magnon—magnon–magnon, **c** cavity–magnon–magnon, and **d** magnon–phonon–magnon configurations, respectively. For these subfigures, the parameters are $\kappa_{ai}/2\pi = 4.7$ MHz and $\kappa_{mi}/2\pi = 1$ MHz. All other parameters are the same with Fig. 4

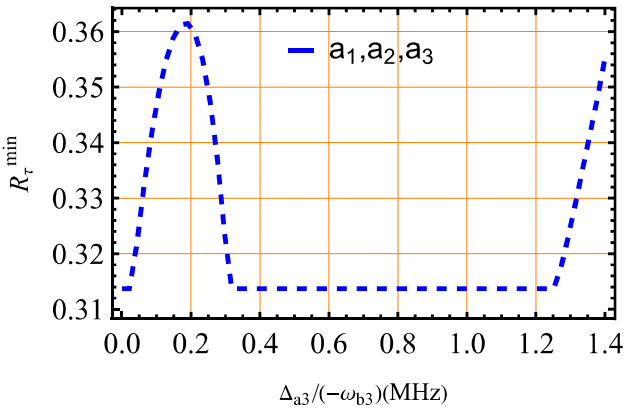

Fig. 6 Plot of the tripartite entanglement R_τ^{min} (cavity–cavity–cavity) as a function of cavity detuning $\Delta_{a3}/(-\omega_{b3})$. The parameters are $\kappa_{ai}/2\pi = 2.0$MHz, $\kappa_{mi}/2\pi = 1$MHz. All other parameters are the same with Fig. 5

3 Results and discussion

In this section, we present and discuss the outcomes for all categories of tripartite entanglement. Our analysis is based on parameters that are experimentally accessible, specifically $\omega_{ai}/2\pi = 10$ GHz, $\omega_{bi}/2\pi = 10$ MHz, $\gamma_{bi}/2\pi = 10^2$ Hz, $g_{mai}/2\pi = 3.2$ MHz, $g_{mbi}/2\pi = 0.2$ Hz, and $B_0 \approx 3.9 \times 10^{-5}$ T. These parameters have previously been employed in a single-cavity configuration, as reported in Refs. [34, 61]. In this study, we extend the same set of values to a three-cavity system to investigate the generation of tripartite entanglement.

To confirm the dynamical viability of our three-cavity magnomechanical system, we perform a comprehensive stability analysis. This involves evaluating the eigenvalue spectrum of the drift matrix **Z**, which governs the linearized dynamics of quantum fluctuations around the system's steady state. Stability is ensured if all eigenvalues of **Z** possess strictly negative real parts, guaranteeing that small perturbations decay over time and that the system relaxes to a unique, stable steady state.

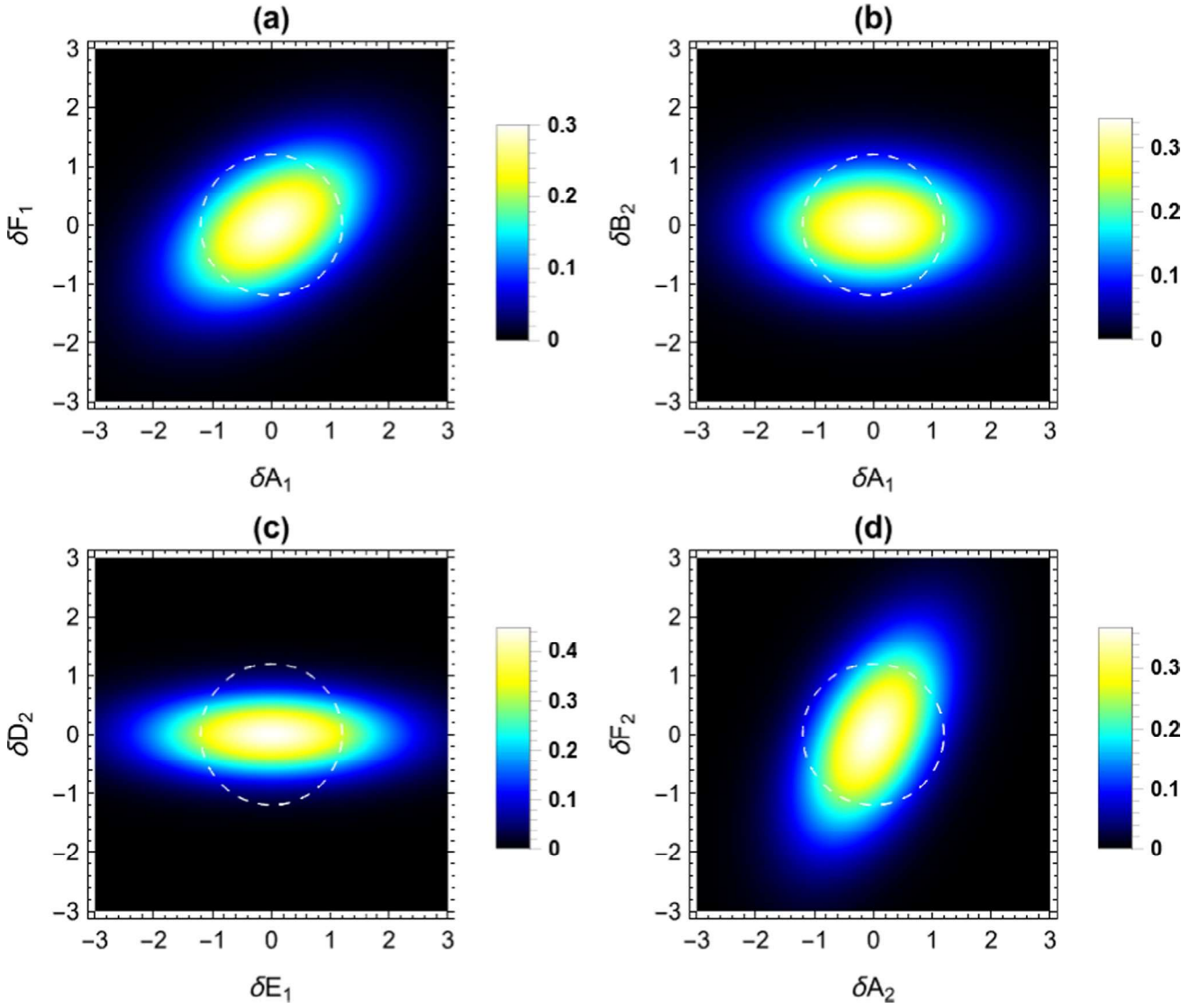

Fig. 7 Wigner function for cross quadrature fluctuations. Sub figure **a**, **b** $\Delta_{a1} = -0.6\omega_{b1}$, $\Delta_{a2} = -\omega_{b2}$, $\Delta_{a3} = -\omega_{b3}$, $\tilde{\Delta}_{m1} = 0.9\omega_{b1}$, $\tilde{\Delta}_{m2} = 0.8\omega_{b2}$, $\tilde{\Delta}_{m3} = 0.8\omega_{b3}$. Sub figure **c** $\tilde{\Delta}_{m2} = -0.9\omega_{b2}$. Sub figure **d** $\tilde{\Delta}_{m1,m2} = -0.9\omega_{b1,b2}$, $\Delta_{m3} = 0.8\omega_{b3}$, $\Delta_{a1} = -0.6\omega_{b1}$, $\Delta_{a2} = -0.4\omega_{b2}$, $\Delta_{a3} = -\omega_{b3}$ for all (**a–d**) the temperature is $T = 10$ mK. All other parameters are the same with Fig. 5

As illustrated in Fig. 2a, the computed real parts of the eigenvalues are entirely confined to the negative half-plane. This confirms the unconditional dynamical stability of the proposed configuration under the chosen set of parameters.

To further assess the robustness of the system's stability under variations in key interaction parameters, we examine how the real parts of the eigenvalues of the drift matrix $\mathbf{Z}$ evolve with the magnomechanical coupling strength g_{mb1}. As shown in Fig. 2b, all eigenvalues maintain strictly negative real parts throughout the entire range of g_{mb1} explored. This persistence of negative real parts demonstrates that the dynamical stability of the system is resilient to changes in the magnomechanical interaction strength, thereby confirming the structural integrity of the proposed configuration under realistic experimental conditions.

To investigate the generation of distributed tripartite entanglement under realistic experimental conditions, we analyze the entanglement measure $R_\tau^{\min}$ as a function of two key tunable parameters: the normalized effective magnon drive detuning $\tilde{\Delta}mi/(0.9\omega bi)$ and the normalized cavity detuning $\Delta_{ai}/(-\omega_{b3})$. The entanglement landscapes for various configurations of hybrid mode triplets are shown in Fig. 3, where the logarithmic negativity criterion is used for evaluation. The chosen parameters for the analysis are: $g_{ma1}/2\pi = 3.2$MHz, $g_{ma2}/2\pi = 3.0$ MHz, $g_{ma3}/2\pi = 3.2$ MHz, $g_{mbi}/2\pi = 0.3$ Hz, $\omega_{bi}/2\pi = 10$ MHz, $\Omega_i = 7.1 \times 10^{14}$Hz, $\Delta_{ai} = -\omega_{bi}$, $\tilde{\Delta}mi = 0.9\omega bi$, and $\gamma_{bi}/2\pi = 100$Hz.

Figure 3 presents a comprehensive analysis of tripartite entanglement across a range of hybrid configurations by plotting the entanglement monotone $R_\tau^{\min}$ as a function of the normalized magnon drive detuning $\tilde{\Delta}m1/(0.9\omega b1)$ and cavity detuning $\Delta_{a3}/(-\omega_{b3})$. Each subplot showcases distinct combinations of magnonic, phononic, and photonic modes, highlighting the system's potential

to generate and sustain multipartite entanglement within a unified framework. Throughout Figs. 3, 4 and 5a, we assume matched dissipation rates, i.e., $\kappa_{a_i} = \kappa_{m_i}$.

Tripartite entanglement between spatially separated magnon modes (m_1, m_2, m_3) is demonstrated in Fig. 3a. Each magnon resides in its own cavity containing a YIG sphere, and although there is no direct coupling between the cavities, a coherent global drive synchronizes the phases of all cavities. This coherence, together with strong local magnon–photon interactions, facilitates indirect entanglement generation among the magnons.

A hybrid triplet configuration involving a cavity mode and two remote magnon modes, (a_1, m_2, m_3), is depicted in Fig. 3b. In this setup, the entanglement arises indirectly from the globally driven cavity fields, which couple locally to their respective magnons. The coherent global drive ensures phase-alignment of the cavity fields, enabling the transfer of quantum information from a_1 to m_2 and m_3 via local couplings.

Shown in Fig. 3c is a mixed hybrid configuration involving two magnon modes and a phonon mode (m_1, b_1, m_2). Strong local bipartite entanglement arises from magnetostrictive coupling between m_1 and b_1 within a single cavity. Meanwhile, m_1 and m_2 become correlated via synchronized cavity drives and photon–magnon coupling chains, linking magnetic and mechanical modes across cavities.

Depicted in Fig. 3d are the cavity modes (a_1, a_2, a_3), which become tripartitely entangled indirectly through magnon-mediated correlations. Each optical mode couples locally to its own YIG sphere, and the entangled magnon network transfers quantum correlations to the cavity fields, effectively enabling entanglement swapping across spatially separated photonic modes.

Next in Fig. 4a, we consider a configuration comprising two cavity modes (a_1, a_2) and a mechanical mode b_3, each located in distinct cavities. While the subsystems are spatially separated, multipartite entanglement arises due to a global coherent drive acting on all cavity modes, combined with strong local photon–magnon and magnon–phonon couplings within each hybrid unit. The phase coherence introduced by the global drive, together with hybrid interaction chains, allows the mechanical mode b_3 to become quantum correlated with remote cavity fields. This generates effective multi-path quantum correlations that mediate entanglement across the network, even without direct Hamiltonian coupling between distant modes.

Figure 4b examines the temperature dependence of entanglement in the magnonic triplet (m_1, m_2, m_3). Here, coherent global driving sustains strong entanglement despite spatial separation. However, thermal decoherence progressively reduces entanglement beyond a critical temperature threshold.

The temperature dependence of the hybrid system (a_1, m_2, m_3) is illustrated in Fig. 4c. The entanglement shows moderate robustness against thermal noise at low temperatures, remaining appreciable up to $T \approx 0.1$ K. This behavior reflects the combined influence of coherent drive, strong local couplings, and dissipation, which enable steady-state entanglement to persist despite increasing thermal fluctuations. Beyond this point, thermal decoherence dominates, reducing the quantum correlations among the subsystems.

Figure 4d focuses on the mixed hybrid system (m_1, b_1, m_2), where entanglement starts from a relatively high value and decays monotonically with increasing temperature, reflecting the sensitivity of such hybrid configurations to thermal fluctuations.

The resilience of photonic entanglement among the three cavity modes (a_1, a_2, a_3) under increasing temperature is explored in Fig. 5a. A gradual decline in coherence is observed, consistent with the thermal degradation trends seen in earlier hybrid configurations.

Tripartite entanglement among the magnon modes (m_1, m_2, m_3) is analyzed in Fig. 5b as a function of magnon detuning for the regime $\kappa_{ai} > \kappa_{mi}$. The results show that the entanglement remains robust, even when cavity dissipation exceeds that of the magnon modes.

Entanglement profiles for the hybrid configurations (a_1, m_2, m_3) and (m_1, b_1, m_2) are shown in Fig. 5c and d, respectively. Both cases demonstrate stable hybrid entanglement across varying magnon detunings under the same dissipation condition, highlighting the effectiveness of magnon-mediated coherence in supporting multipartite correlations.

A complementary view is offered in Fig. 6, which presents the tripartite entanglement among optical cavity modes (a_1, a_2, a_3) as a function of the cavity detuning. Conducted within the regime $\kappa_{ai} > \kappa_{mi}$, this analysis reveals a persistent yet modest entanglement level, emphasizing the capacity for sustaining photonic coherence even when optical losses dominate.

To investigate the effect of cavity–magnon detunings on two-mode squeezing between cross-quadrature pairs, we reconstruct the Wigner function, denoted as $W(\psi)$, which offers a quasi-probability distribution in phase space and serves as a powerful tool for visualizing nonclassical phenomena such as squeezing and entanglement. The reconstructed Wigner functions are analyzed for various quadrature combinations within the cavity–magnonic system.

As the configuration depicted in Fig. 1, the selective enhancement of spatial quantum correlations and efficient interfacing of entangled optical fields with collective magnonic excitations. The corresponding phase-space Wigner projections reveal the sensitivity of two-mode squeezing to detuning parameters and external field configurations. To this end, we construct the Wigner function, defined as

$$W(\psi) = \frac{\exp\left(-\frac{1}{2}\psi V^{-1}\psi^{\dagger}\right)}{\pi^2\sqrt{\det V}}, \tag{47}$$

where ψ denotes the state vector containing the fluctuation quadratures of two selected modes, and V is the corresponding reduced covariance matrix.

Figure 7a–d displays representative projections of the Wigner function $W(\psi)$ for various cross-quadrature pairs: δA_1, δF_1, δA_1, δB_2, δE_1, δD_2, and δA_2, δF_2, respectively.

In subfigures (a) and (b), the cavity detunings are set to $\Delta_{a1} = -0.6$, ω_{b1}, $\Delta_{a2} = -\omega_{b2}$, and $\Delta_{a3} = -\omega_{b3}$, while the magnon detunings are chosen as $\tilde{\Delta}m1 = 0.9$, $\omega b1$, $\tilde{\Delta}m2 = 0.8$, $\omega b2$, and $\tilde{\Delta}m3 = 0.8$, $\omega b3$. These moderately red-detuned parameters enable strong photon–magnon hybridization via beam-splitter-type interactions. As a result, the Wigner distributions in (a) and (b) exhibit pronounced elliptical squeezing along the cross-quadrature axes, a hallmark of nonclassical correlations generated through coherent optomagnonic coupling.

In contrast, Fig. 7c involves a significantly altered magnon detuning $\tilde{\Delta}m2 = -0.9$, $\omega b2$, pushing the system into a highly dispersive regime. This configuration was initially anticipated to yield degraded coherence and increased thermal noise, thereby producing a more isotropic and thermal-like Wigner profile. However, the actual distribution remains distinctly elliptical and squeezed—arguably more so than in (a) and (b). This unexpected squeezing suggests that nontrivial quantum correlations persist even in this strongly detuned regime, possibly due to residual indirect coupling pathways or mode mixing facilitated by the multimode mechanical bus. The anisotropic shape of the Wigner function in this case highlights the complexity of hybrid-mode dynamics, where suppression of direct coherence does not necessarily eliminate squeezing, but can redistribute it in phase space.

Figure 7d explores an alternative configuration with strongly red-detuned magnons $\tilde{\Delta}m1 = \tilde{\Delta}m2 = -0.9$, $\omega_{b1,b2}$, and cavity detunings $\Delta_{a1} = -0.6$, ω_{b1}, $\Delta_{a2} = -0.4$, ω_{b2}, $\Delta_{a3} = -\omega_{b3}$, along with $\tilde{\Delta}m3 = 0.8$, $\omega b3$. This configuration reestablishes strong hybridization across optical and magnonic modes, particularly via the mechanical interface, enabling renewed spatial correlations and leading to clear elliptical squeezing in the Wigner projection. The emergence of this nonclassical structure confirms the reactivation of hybrid-mode entanglement under favorable detuning balance.

Across all panels, the temperature is maintained at $T = 10$, mK, and other parameters are consistent with those used in Fig. 3. These results collectively underscore the pivotal role of magnon detuning in modulating the nature and directionality of hybrid entanglement. The rich variety in Wigner function structures, from elliptical squeezing to near-thermal distributions, reflects the delicate interplay between detuning, coherence, and quantum backaction in multimode cavity–magnon–phonon systems.

It is important to emphasize that, although the three cavities are not directly coupled, the multipartite entanglement observed in our scheme is enabled by injecting a shared nonclassical resource and subsequently redistributing it through purely local hybrid interactions. Specifically, the tripartite entangled probe fields are generated by a common SPDC source based on a nonlinear BBO crystal and are then independently injected into three spatially separated optical cavities. The initial intermode quantum correlations carried by these inputs are converted and reconfigured into magnon–photon–phonon entanglement via the driven–dissipative dynamics within each cavity–magnon–phonon subsystem. This resource-conversion mechanism is fundamentally different from entanglement generation based on coherent (Hamiltonian) inter-cavity coupling, and it remains robust under realistic conditions, including moderate thermal noise and finite frequency detunings. Consequently, our results demonstrate that steady-state tripartite entanglement can be achieved in a fully distributed architecture without any direct inter-system couplings by combining externally prepared nonclassical inputs with local hybrid interactions in an open-system setting. This provides a scalable and versatile route toward continuous-variable quantum networks, distributed quantum memories, and hybrid quantum interfaces for quantum information processing and sensing.

4 Conclusion

In this work, we have proposed and analyzed a theoretically feasible scheme for generating distributed tripartite entanglement in a network of three spatially separated cavity–magnon–phonon units, each realized by embedding a YIG sphere in an individual microwave cavity. The hybrid subsystems are not directly coupled; instead, nonclassical three-mode entangled probe fields, generated by a common nonlinear SPDC source, are injected into the cavities and converted into hybrid magnon—photon–phonon correlations.

Within a linearized quantum Langevin framework, we solved the Lyapunov equation for the steady-state covariance matrix and confirmed dynamical stability over a broad parameter range via the eigenvalues of the drift matrix. The resulting Gaussian steady states exhibit robust tripartite entanglement among different combinations of magnons, photons, and phonons, quantified by the minimum residual contangle $R_\tau^{\min}$ and the logarithmic negativity. The entanglement persists under realistic levels of thermal noise and cavity loss, indicating resilience compatible with near-term experiments. In addition, two-mode squeezing of cross-quadratures, visible in the Wigner function distributions, highlights the crucial role of detuning and coupling parameters in tailoring the entanglement structure.

These results demonstrate how externally prepared nonclassical resources can be distributed and reshaped in a modular magnomechanical platform, providing a promising route toward scalable continuous-variable quantum networks, distributed quantum memories, and hybrid quantum interfaces for information processing and transduction.

Acknowledgements The authors, Saud Owyed, express their gratitude to the Deanship of Scientific Research at the University of Bisha for funding this research through the general research project under grant number (UB-GRP-20-1444). Pei Zhang acknowledges the support received from the National Natural Science Foundation of China (Grant No. 12174301), the Natural Science Basic Research Program of Shaanxi (Program No. 2023-JC-JQ-01), and the Fundamental Research Funds for the Central Universities.

Data Availability statements The manuscript has associated data in a data repository.

Appendix

The expressions used in Eq. (42) are given by the following

$$u = [\mathcal{X}, \mathcal{Y}, \mathcal{Z}]^T \tag{48}$$

with

$$\mathcal{X} = \delta A_1(t),\ \delta B_1(t),\ \delta C_1(t),\ \delta D_1(t),\ \delta E_1(t),\ \delta F_1(t),$$
$$\mathcal{Y} = \delta A_2(t),\ \delta B_2(t),\ \delta C_2(t),\ \delta D_2(t),\ \delta E_2(t),\ \delta F_2(t),$$
$$\mathcal{Z} = \delta A_3(t),\ \delta B_3(t),\ \delta C_3(t),\ \delta D_3(t),\ \delta E_3(t),\ \delta F_3(t)$$

and

$$n = [\mathcal{X}_1, \mathcal{Y}_1, \mathcal{Z}_1]^T \tag{49}$$

with

$$\mathcal{X}_1 = \sqrt{2\kappa_{a1}}A_1^{\text{in}}(t),\ \sqrt{2\kappa_{a1}}B_1^{\text{in}}(t),\ \sqrt{2\kappa_{m1}}C_1^{\text{in}}(t),\ \sqrt{2\kappa_{m1}}D_1^{\text{in}}(t),\ \sqrt{2\gamma_{b1}}E_1^{\text{in}}(t),\ \sqrt{2\gamma_{b1}}F_1^{\text{in}}(t)$$
$$\mathcal{Y}_1 = \sqrt{2\kappa_{a2}}A_2^{\text{in}}(t),\ \sqrt{2\kappa_{a2}}B_2^{\text{in}}(t),\ \sqrt{2\kappa_{m2}}C_2^{\text{in}}(t),\ \sqrt{2\kappa_{m2}}D_2^{\text{in}}(t),\ \sqrt{2\gamma_{b2}}E_2^{\text{in}}(t),\ \sqrt{2\gamma_{b2}}F_2^{\text{in}}(t)$$
$$\mathcal{Z}_1 = \sqrt{2\kappa_{a3}}A_3^{\text{in}}(t),\ \sqrt{2\kappa_{a3}}B_3^{\text{in}}(t),\ \sqrt{2\kappa_{m3}}C_3^{\text{in}}(t),\ \sqrt{2\kappa_{m3}}D_3^{\text{in}}(t),\ \sqrt{2\gamma_{b3}}E_3^{\text{in}}(t),\ \sqrt{2\gamma_{b3}}F_3^{\text{in}}(t)$$

where Z is the drift matrix, which can be extracted from the coefficients of the vector in Eqs. (35)–(40).

The drift matrix can be written as:

$$Z_{18,18} = \begin{pmatrix} x_{1,1} & x_{1,2} & \cdots & x_{1,18} \\ x_{2,1} & x_{2,2} & \cdots & x_{2,18} \\ \vdots & \vdots & \ddots & \vdots \\ x_{18,1} & x_{18,2} & \cdots & x_{18,18} \end{pmatrix},$$

In the above matrix Z, all other elements are zero, except for the following, which are relevant to this system:

$$x_{1,1} = -\kappa_{a1}, \quad x_{1,2} = \Delta_{a1}, \quad x_{1,4} = g_{ma1}, \tag{50}$$
$$x_{2,1} = -\Delta_{a1}, \quad x_{2,2} = -\kappa_{a1}, \quad x_{2,3} = -g_{ma1}, \tag{51}$$
$$x_{3,2} = g_{ma1}, \quad x_{3,3} = -\kappa_{m1}, \quad x_{3,4} = \tilde{\Delta}_{m1}, \tag{52}$$
$$x_{4,1} = -g_{ma1}, \quad x_{4,3} = -\tilde{\Delta}_{m1}, \tag{53}$$
$$x_{4,4} = -\kappa_{m1}, \quad x_{4,5} = -2g_{mb1}\alpha_1, \tag{54}$$
$$x_{5,4} = g_{mb1}(\alpha_1^* - \alpha_1), \quad x_{5,5} = -\gamma_{b1}, \quad x_{5,6} = \omega_{b1}, \tag{55}$$
$$x_{6,3} = -g_{mb1}(\alpha_1^* + \alpha_1), \quad x_{6,5} = -\omega_{b1}, \quad x_{6,6} = -\gamma_{b1}, \tag{56}$$
$$x_{7,7} = -\kappa_{a2}, \quad x_{7,8} = \Delta_{a2}, \quad x_{7,10} = g_{ma2}, \tag{57}$$
$$x_{8,7} = -\Delta_{a2}, \quad x_{8,8} = -\kappa_{a2}, \quad x_{8,9} = -g_{ma2}, \tag{58}$$
$$x_{9,8} = g_{ma2}, \quad x_{9,9} = -\kappa_{m2}, \quad x_{9,10} = \tilde{\Delta}_{m2}, \tag{59}$$
$$x_{10,7} = -g_{ma2}, \quad x_{10,9} = -\tilde{\Delta}_{m2}, \tag{60}$$
$$x_{10,10} = -\kappa_{m2}, \quad x_{10,11} = -2g_{mb2}\alpha_2, \tag{61}$$
$$x_{11,10} = g_{mb2}(\alpha_2^* - \alpha_2), \quad x_{11,11} = -\gamma_{b2}, \quad x_{11,12} = \omega_{b2}, \tag{62}$$
$$x_{12,9} = -g_{mb2}(\alpha_2^* + \alpha_2), \quad x_{12,11} = -\omega_{b2}, \quad x_{12,12} = -\gamma_{b2}, \tag{63}$$
$$x_{13,13} = -\kappa_{a3}, \quad x_{13,14} = \Delta_{a3}, \quad x_{13,16} = g_{ma3}, \tag{64}$$

$$x_{14,13} = -\Delta_{a3}, \quad x_{14,14} = -\kappa_{a3}, \quad x_{14,15} = -g_{ma3}, \tag{65}$$

$$x_{15,14} = g_{ma3}, \quad x_{15,15} = -\kappa_{m3}, \quad x_{15,16} = \tilde{\Delta}_{m3}, \tag{66}$$

$$x_{16,13} = -g_{ma3}, \quad x_{16,15} = -\tilde{\Delta}_{m3}, \tag{67}$$

$$x_{16,16} = -\kappa_{m3}, \quad x_{16,17} = -2g_{mb3}\alpha_3, \tag{68}$$

$$x_{17,16} = g_{mb3}(\alpha_3^* - \alpha_3), \quad x_{17,17} = -\gamma_{b3}, \quad x_{17,18} = \omega_{b3}, \tag{69}$$

$$x_{18,15} = -g_{mb3}(\alpha_3^* + \alpha_3), \quad x_{18,17} = -\omega_{b3}, \quad x_{18,18} = -\gamma_{b3}. \tag{70}$$

The diffusion matrix is given by

$$D_{18,18} = \begin{pmatrix} e_{1,1} & e_{1,2} & \cdots & e_{1,18} \\ e_{2,1} & e_{2,2} & \cdots & e_{2,18} \\ \vdots & \vdots & \ddots & \vdots \\ e_{18,1} & e_{18,2} & \cdots & e_{18,18} \end{pmatrix},$$

From the above matrix D for simplification we mention its diagonal elements dia and other nonzero elements as

$$\begin{aligned} \text{dia} =& (\kappa_{a1}^{'}, \kappa_{a1}^{'}, \kappa_{m1}, \kappa_{m1}, \gamma_{b1}, \gamma_{b1}, \kappa_{a2}^{'}, \kappa_{a2}^{'}, \\ & \kappa_{m2}, \kappa_{m2}, \gamma_{b2}, \gamma_{b2}, \kappa_{a3}^{'}, \kappa_{a3}^{'}, \kappa_{m3}, \kappa_{m3}, \\ & \gamma_{b3}, \gamma_{b3}) \end{aligned} \tag{71}$$

$$e_{1,7} = \kappa_{a2}\mathcal{M}_{1,2}, \; e_{1,13} = \kappa_{a3}\mathrm{M}_{3,1}, \; e_{2,8} = -\kappa_{a2}\mathcal{M}_{1,2}$$

$$e_{2,14} = -\kappa_{a3}\mathcal{M}_{3,1}, \; e_{7,1} = \kappa_{a1}\mathrm{M}_{1,2}, \; e_{7,13} = \kappa_{a3}\mathcal{M}_{2,3}$$

$$e_{8,2} = -\kappa_{a1}\mathcal{M}_{1,2}, \; e_{8,14} = -\kappa_{a3}\mathrm{M}_{2,3}, \; e_{13,1} = \kappa_{a1}\mathcal{M}_{3,1}$$

$$e_{13,7} = \kappa_{a2}\mathcal{M}_{2,3}, \; e_{14,2} = -\kappa_{a1}\mathrm{M}_{3,1}, \; e_{14,8} = -\kappa_{a2}\mathcal{M}_{2,3}$$

Here $\kappa_{ai}^{'} = \kappa_{ai}(\mathcal{N}_{ai} + 1/2)$.

References

1. R. Macêdo, R. Holland, P. Baity, L. Mclellan, K. Livesey, R. Stamps, M. Weides, D. Bozhko, Phys. Rev. Appl. **15**(2), 024065 (2021). https://doi.org/10.1103/PhysRevApplied.15.024065
2. J.-X. Peng, B. Zhu, W. Zhang, K. Zhang, Phys. Rev. A **109**, 022601 (2024). https://doi.org/10.1103/PhysRevA.109.022601
3. J.-X. Han, J.-L. Wu, Z.-H. Yuan, Y.-J. Chen, Y. Xia, Y.-Y. Jiang, J. Song, Phys. Rev. Appl. **21**, 014057 (2024). https://doi.org/10.1103/PhysRevApplied.21.014057
4. L.-L. Zheng, W. Shi, K. Shen, D. Kong, F. Wang, Opt. Expr. **31**(20), 32953–32967 (2023). https://doi.org/10.1364/OE.493946
5. D. Hatanaka, M. Asano, H. Okamoto, Y. Kunihashi, H. Sanada, H. Yamaguchi, Phys. Rev. Appl. **17**(3), 034024 (2022). https://doi.org/10.1103/PhysRevApplied.17.034024
6. K. Mukherjee, P. Jana, J. Korean Phys. Soc. **82**(4), 356–363 (2022). https://doi.org/10.1007/s40042-022-00677-7
7. J. Xu, C. Zhong, X. Han, D. Jin, L. Jiang, X. Zhang, Phys. Rev. Lett. **125**, 237201 (2020). https://doi.org/10.1103/PhysRevLett.125.237201
8. X. Zhang, C.-L. Zou, L. Jiang, H.X. Tang, Phys. Rev. Lett. **113**, 156401 (2014). https://doi.org/10.1103/PhysRevLett.113.156401
9. A.A. Serga, A.V. Chumak, B. Hillebrands, J. Phys. D Appl. Phys. **43**, 264002 (2010). https://doi.org/10.1088/0022-3727/43/26/264002
10. C. Kong, X. Bao, J. Liu, H. Xiong, Opt. Expr. **29**(16), 25477 (2021) https://api.semanticscholar.org/CorpusID:237726417
11. A.V. Chumak, A.A. Serga, B. Hillebrands, Nat. Commun. **5**, (2014) https://api.semanticscholar.org/CorpusID:12225558
12. C. Kittel, Phys. Rev. **73**, 155 (1948). https://doi.org/10.1103/PhysRev.73.155
13. M. Goryachev, W.G. Farr, D.L. Creedon, Y. Fan, M. Kostylev, M.E. Tobar, Phys. Rev. Appl. **2**, 054002 (2014). https://doi.org/10.1103/PhysRevApplied.2.054002
14. L. Bai, M. Harder, Y.P. Chen, X. Fan, J.Q. Xiao, C.-M. Hu, Phys. Rev. Lett. **114**, 227201 (2015). https://doi.org/10.1103/PhysRevLett.114.227201
15. E. Schrödinger, Math. Proc. Cambridge Philos. Soc. **31**, 555 (1935) https://api.semanticscholar.org/CorpusID:121278681
16. D. Bouwmeester, A. K. Ekert, and A. Zeilinger (2000)
17. N. Zou, J. Phys: Conf. Ser. **1827**, 012120 (2021). https://doi.org/10.1088/1742-6596/1827/1/012120
18. J.S. Bell, Phys. Physique Fizika **1**, 195 (1964). https://doi.org/10.1103/PhysicsPhysiqueFizika.1.195
19. M. Aspelmeyer, T.J. Kippenberg, F. Marquardt, Rev. Mod. Phys. **86**, 1391 (2014). https://doi.org/10.1103/RevModPhys.86.1391
20. D. Vitali, S. Gigan, A. Ferreira, H. Boehm, P. Tombesi, A. Guerreiro, V. Vedral, A. Zeilinger, M. Aspelmeyer, Phys. Rev. Lett. **98**(3), 030405 (2006). https://doi.org/10.1103/PhysRevLett.98.030405
21. L.-L. Zhai, H.-J. Du, J.-L. Guo, Quant. Inf. Process. (2023). https://doi.org/10.1007/s11128-023-03965-8
22. S.-X. Wu, C.-H. Bai, G. Li, C.-S. Yu, T. Zhang, Opt. Express **32**, 1 (2023). https://doi.org/10.1364/OE.510160
23. C. Jiang, H. Lu, Z. Zhai, G. Chen, Photonics **9**, 818 (2022). https://doi.org/10.3390/photonics9110818

24. X. Yang, H. Yin, F. Zhang, J. Nie, Laser Phys. Lett. **20**, 015205 (2022). https://doi.org/10.1088/1612-202X/aca97a
25. D. Aoune, B. Noureddine, N. Habiballah, M. Nassik, Int. J. Mod. Phys. B **38**(04), 2450053 (2023). https://doi.org/10.1142/S021797922450053X
26. L. Zigeng, X. Li, X. Zhong, Opt. Express **31**(12), 19382–19391 (2023). https://doi.org/10.1364/OE.488948
27. L. Youness, B. Maroufi, M. Daoud, Mod. Phys. Lett. A **38**(34n35), 2350154 (2023). https://doi.org/10.1142/S0217732323501547
28. J.-D. Tang, Q.-Z. Cai, C. Ze-di, N. Xu, G.-Y. Peng, P.-Q. Chen, D.-G. Wang, Z.-W. Xia, Y. Wang, H.-Z. Song, Q. Zhou, D. Guangwei, Phys. Lett. A **429**, 127966 (2022). https://doi.org/10.1016/j.physleta.2022.127966
29. D. Vitali, S. Mancini, P. Tombesi, Phys. Rev. A **64**, 051401 (2001). https://doi.org/10.1103/PhysRevA.64.051401
30. A.A. Geraci, S.B. Papp, J. Kitching, Phys. Rev. Lett. **105**, 101101 (2010). https://doi.org/10.1103/PhysRevLett.105.101101
31. P. Fritschel, Adv. Gravit. Wave Detect. **113**, 1 (2012). https://doi.org/10.1017/CBO9781139046916.009
32. R. Riedinger, A. Wallucks, I. Marinkovic, C. Löschnauer, M. Aspelmeyer, S. Hong, S. Gröblacher, Nature **556**(7702), 473–477 (2018). https://doi.org/10.1038/s41586-018-0036-z
33. S. Barzanjeh, A. Xuereb, S. Groeblacher, M. Paternostro, C. Regal, E. Weig, Nat. Phys. **18**(1), 15–24 (2021). https://doi.org/10.1038/s41567-021-01402-0
34. J. Li, S.-Y. Zhu, G.S. Agarwal, Phys. Rev. Lett. **121**, 203601 (2018). https://doi.org/10.1103/PhysRevLett.121.203601
35. J. Li, S.-Y. Zhu, New J. Phys. **21**(8), 085001 (2019). https://doi.org/10.1088/1367-2630/ab3508
36. B. Hussain, S. Qamar, M. Irfan, Phys. Rev. A (2022). https://doi.org/10.1103/PhysRevA.105.063704
37. Z. Zhang, M.O. Scully, G.S. Agarwal, Phys. Rev. Res. **1**, 023021 (2019). https://doi.org/10.1103/PhysRevResearch.1.023021
38. Z.-B. Yang, J.-S. Liu, H. Jin, Q.-H. Zhu, A.-D. Zhu, H.-Y. Liu, Y. Ming, Y. Rong-Can, Opt. Express **28**, 31862 (2020). https://doi.org/10.1364/OE.404522
39. X. Ji, X. Yang, J. Condens, Matter Phys. **36**, 243001 (2024). https://doi.org/10.1088/1361-648X/ad2c73
40. X. Ji, H. Geng, N. Akhtar, X. Yang, Phys. Rev. B **111**, 195419 (2025). https://doi.org/10.1103/PhysRevB.111.195419
41. X. Zhang, N. Zhu, C.-L. Zou, H.X. Tang, Phys. Rev. Lett. **117**, 123605 (2016). https://doi.org/10.1103/PhysRevLett.117.123605
42. G.-Q. Zhang, J.Q. You, Phys. Rev. B **99**, 054404 (2019). https://doi.org/10.1103/PhysRevB.99.054404
43. L. Bai, M. Harder, P. Hyde, Z. Zhang, C.-M. Hu, Y.P. Chen, J.Q. Xiao, Phys. Rev. Lett. **118**, 217201 (2017). https://doi.org/10.1103/PhysRevLett.118.217201
44. Y.-P. Wang, G.-Q. Zhang, D. Zhang, T.-F. Li, C.-M. Hu, J.Q. You, Phys. Rev. Lett. **120**, 057202 (2018). https://doi.org/10.1103/PhysRevLett.120.057202
45. J. Li, S.-Y. Zhu, G.S. Agarwal, Phys. Rev. A **99**, 021801 (2019). https://doi.org/10.1103/PhysRevA.99.021801
46. W. Zhang, T. Wang, H. Xue, S. Zhang, H.-F. Wang, Opt. Express **30**(7), 10969–10980 (2022). https://doi.org/10.1364/OE.453787
47. H.Y. Yuan, S. Zheng, Z. Ficek, Q.Y. He, M.-H. Yung, Phys. Rev. B **101**, 014419 (2020). https://doi.org/10.1103/PhysRevB.101.014419
48. D. Ming Song, L. Zheng, Y. Shi, Y. Liu, J. Opt. Soci. Am. B **39**(10), 2665–2669 (2022). https://doi.org/10.1364/JOSAB.465554
49. M.-C. Li, A.-X. Chen, W. Zeng, Open Phys. **21**(1), 20220240 (2023). https://doi.org/10.1515/phys-2022-0240
50. W. Qiu, X. Cheng, A. Chen, Y. Lan, W. Nie, Phys. Rev. A **105**(6), 063718 (2022). https://doi.org/10.1103/PhysRevA.105.063718
51. A. Sohail Shah, J.-X. Peng, A. Hidki, M. Khalid, S. Singh, Sci. Rep. **13**, 21840 (2023a). https://doi.org/10.1038/s41598-023-48825-8
52. A. Sohail Shah, R. Ahmed, J.-X. Peng, A. Shahzad, S. Singh, J. Opt. Soci. Am. B. **40**(5), 1359–1366 (2023). https://doi.org/10.1364/JOSAB.484943
53. J. Wang, Quant. Inf. Process. **21**(3), 105 (2022). https://doi.org/10.1007/s11128-022-03438-4
54. B. Hussain, S. Qamar, M. Irfan, Phys. Rev. A **105**, 063704 (2022b). https://doi.org/10.1103/PhysRevA.105.063704
55. K. Di, S. Tan, L. Wang, A. Cheng, X. Wang, Y. Liu, J. Du, Opt. Expr. **31**, 29491 (2023)
56. S.Q. Dilawaiz, M. Irfan, Phys. Rev. A **109**, 043708 (2024). https://doi.org/10.1103/PhysRevA.109.043708
57. X. Zhang, C.-L. Zou, L. Jiang, H. Tang, Sci. Adv. **2**, 1 (2015a) https://doi.org/10.1126/sciadv.1501286
58. T. Holstein, H. Primakoff, Phys. Rev. **58**, 1098 (1940). https://doi.org/10.1103/PhysRev.58.1098
59. J. Li, S.-Y. Zhu, G. Agarwal, Phys. Rev. Lett. **121**, 203601 (2018b). https://doi.org/10.1103/PhysRevLett.121.203601
60. X. Zhang, C.-L. Zou, L. Jiang, H. Tang, Sci. Adv. **2**(3), e1501286 (2015b). https://doi.org/10.1126/sciadv.1501286
61. M. Amazioug, B. Teklu, M. Asjad, Sci. Rep. **13**(1), 3833 (2023). https://doi.org/10.1038/s41598-023-30693-x
62. R. Benguria, M. Kac, Phys. Rev. Lett. **46**, 1 (1981). https://doi.org/10.1103/PhysRevLett.46.1
63. H.I. Nurdin, IEEE Control Syst. Lett. **9**, 1009 (2025)
64. V. Giovannetti, D. Vitali, Phys. Rev. A **63**, 023812 (2001). https://doi.org/10.1103/PhysRevA.63.023812
65. M.B. Plenio, Phys. Rev. Lett. **95**, 090503 (2005). https://doi.org/10.1103/PhysRevLett.95.090503
66. G. Adesso, F. Illuminati, J. Phys. A: Math. Theor. **40**, 7821 (2007). https://doi.org/10.1088/1751-8113/40/28/S01
67. G. Adesso, A. Serafini, F. Illuminati, Phys. Rev. A **70**, 022318 (2004). https://doi.org/10.1103/PhysRevA.70.022318